

Identification of hidden mineralized and non-mineralized zones using spectral analysis of geochemical data

Hossein Mahdiyanfar ^{a,*}, Mohammad Farzamian ^b

^a Department of Mining Engineering, University of Gonabad, Gonabad, Iran

^b Centro de Geofísica, Universidade de Lisboa, Campo Grande Ed. C8, 1749-016 Lisbon, Portugal

Article History:

Received: 06 January 2019,

Revised: 16 July 2019,

Accepted: 02 April 2020.

ABSTRACT

Detection of dispersed and blind mineral deposits is an important aim in the mineral exploration. Detailed exploratory operations such as drilled boreholes which are performed for exploration of mineral deposits in the depth caused high cost and risk. In this research, a new scenario based on spectral analysis of geochemical data has been utilized for prediction of mineralized zones in the depth without any additional cost. The variations of mineralized elements from the surface to the depth are predicted and delineated by using this approach based on surface geochemical data. This proposed approach is the state-of-the-art application of two-dimensional Fourier transformation (2DFT) for geochemical image processing. This approach which is named frequency coefficient method (FCM) has been defined based on the behavior of elements in the frequency domain. In this study, the FCM shows two Pb and Zn mineralized zones at the surface and moderate depth and a non-mineralized zone at the profound depth in Chichakloo Pb–Zn mineralization. Finally, the results of FCM have been validated and confirmed by the results of drilled boreholes and geophysical surveys.

Keywords: *Dispersed mineralization, Deep mineralization, Geochemical patterns, Geochemical frequency domain, Two-dimensional Fourier transformation*

1. Introduction

The interpretation of surface geochemical data was done in the spatial domain and the frequency domain. The surface geochemical frequency data was surveyed less than the spatial domain of geochemical data in exploratory studies. Various geochemical patterns can be detected using the interpretation of geochemical power spectrum (PS) distribution map. The separation of geochemical anomaly from the background has also been performed in the frequency domain using the power spectrum-area fractal method [1-11]. Wang and Zuo used the trend surface and the fractal method in the geochemical frequency domain for anomaly separation [12]. Wang and Zuo offered a geochemical data processing program in the spatial and frequency domains [13]. Shahi et al. predicted the mineral deposit model using the frequency domain of surface geochemical data and demonstrated the new exploratory information may not be obtained from the spatial domain of geochemical data which can be achieved from the frequency domain [14-17].

The identification of concealed ore deposits and false surface anomalies is an important issue in the geochemical exploration. The absence or presence of the mineral deposits in the depth can be slightly predicted using the descriptions of geological and geochemical features of mineralization type in the spatial domain [18, 19]. The concealed mineralization zones can be detected using the ore deposit type and the characteristics of geochemical haloes can be predicted using the ore deposit models [20]. The geochemical zonality method was introduced for determining the erosion surface and predicting the existence of concealed ore deposits [21, 22]. This method cannot delineate the variations of mineralization elements from the surface to the depth,

based on the surface geochemical data.

Shahi et al. described the worthy relationship between the surface geochemical frequency signals and the situation of mineral deposits in the depth. They showed the low frequency signals in the surface geochemical data are created by the geochemical background values and the deep mineral deposits, while the high geochemical frequency signals are related to the surface mineral deposits and the geochemical noises [14-17]. Shahi et al. delineated the variations of mineralization in the depth using the spectral analysis of surface geochemical data [15, 17]. The geochemical enrichments and depletions in the surface may be caused by the ore deposits in various depths. The mineralized and non-mineralized zones in the depth can be determined using the recognition of these frequency signals. The geochemical background and the deep mineral deposits create the low concentrations of elements in the surface that are related to the very low geochemical frequency signals while the surface mineral deposits and the geochemical noises may cause the high frequency signals in the surface geochemical data [14-17]. In this paper, the frequency coefficients method (FCM) was successfully applied for prediction of Chichakloo Pb – Zn mineral deposit model and detection of concealed mineralized and non-mineralized zones in the depth. FCM is a developed approach based on the PS distribution map and the spectral analysis of elements. The obtained results were validated using geophysical surveys and drilled boreholes.

2. Methodology

The Fourier transform is a useful signal processing approach that decomposes signals based on the sinusoidal functions. It transforms the spatial and temporal signals to the frequency domain and decomposes their frequencies [23]. The various frequencies can be extracted from two

* Corresponding author. Tel: +98-5157229702. E-mail address: hssn.shahi@gmail.com (H. Mahdiyanfar).

dimensional spatial signals using the two-dimensional Fourier transformation (2DFT). The 2DFT can be accomplished on two-dimensional array of data. The 2DFT of one image with two-dimensional array of data was schematically illustrated in Fig. 1. This image shows a t' and t'' dimension. In the first step, one-dimensional Fourier transformation (1DFT) is accomplished on the image in the t' dimension. The first set of Fourier transformation is performed to yield a f' by t'' set of data. Then 1DFT was applied in the t'' dimension to yield a f'' by f' set of data [24].

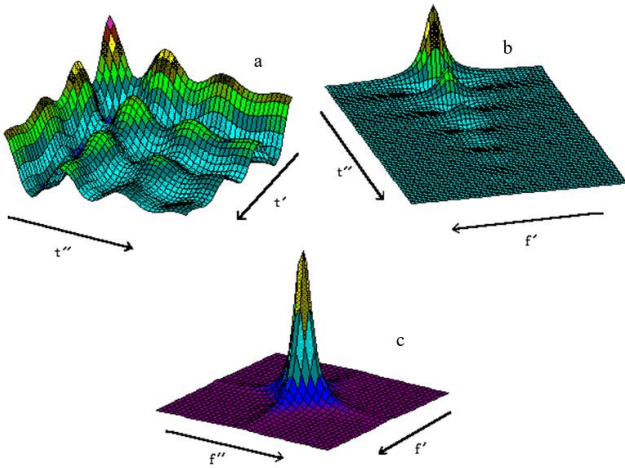


Fig. 1. 2DFT of images, a: Image shows a t' and a t'' dimension. b: 1DFT was performed on the image in the t' dimension. c: 1DFT was performed in the t'' dimension to yield a f' by f'' set of data.

The 2DFT can also be presented mathematically. Dobrin and Savit introduced the equations 1, 2 and 3 for 2DFT [25]. The continues $f(x, y)$ function can be transformed to the frequency domain using the Fourier transformation. The $f(x, y)$ function can be the two-dimensional temporal or the spatial signal [26]. Firstly, the $f(x, y)$ function is transformed based the x variable and y is assumed to be a constant number and in the next step, the obtained function is transformed again based the y variable using 1DFT (Eq. 1). In fact, 2DFT is computed as the series of one-dimensional transforms [25].

$$F_2f(\alpha, \beta) = \int_{-\infty}^{\infty} \left\{ \int_{-\infty}^{\infty} f(x, y) e^{-i\alpha x} dx \right\} e^{-i\beta y} dy \quad (1)$$

In fact, we apply the bellow equation for 2DFT of $f(x, y)$ function:

$$F(K_x, K_y) = \int_{-\infty}^{\infty} \int_{-\infty}^{\infty} f(x, y) \cos(K_x x + K_y y) dx dy \quad (2)$$

$$-i \int_{-\infty}^{\infty} \int_{-\infty}^{\infty} f(x, y) \sin(K_x x + K_y y) dx dy$$

The continues $f(x, y)$ function is the geochemical distribution map of elements in this study and K_x and K_y are "wave numbers" in directions of the east-west and the north-south. Therefore the surface geochemical distribution map as a $f(x, y)$ function can be transformed to $F(K_x, K_y)$ function using this formula. This equation transforms the geochemical distribution map to the real, $R(K_x, K_y)$, and the imaginary, $I(K_x, K_y)$, components in the frequency domain.

Wave number is the spatial counterpart of frequency increasing proportionally to wavelengths as bellow:

$$\lambda_x = 2\pi / K_x, \quad \lambda_y = 2\pi / K_y, \quad (3)$$

$$\lambda = 2\pi \sqrt{(1/K_x^2 + 1/K_y^2)}$$

The PS as an intensity characteristic of the spatial signal is calculated as bellow [26]:

$$E(K_x, K_y) = R^2(K_x, K_y) + I^2(K_x, K_y) \quad (4)$$

Finally, the geochemical distribution map in the spatial domain is

converted to the PS values and the wave numbers in directions of x , the east-west, and y , the north-south, in the frequency domain. The geochemical data in the spatial domain contains various signals with different frequencies [9]. We can interpret the surface geochemical data in the frequency domain using 2DFT [5, 6, 11, 17].

FCM is an effective technique based on the PS distribution of elements and the principal component analysis (PCA). There is a significant relationship between the surface geochemical distribution of elements and the depth of ore deposits that can be detected using FCM. At first, Shahi et al. (2016) presented this approach for detection of deep mineralization. They applied this method properly to interpret the frequency signals of the surface geochemical distribution map [17]. The relationship between the spectral distribution of elements in the surface and the situation of the mineral deposits in the depth is investigated by FCM. FCM can identify the blind and disperse mineralization zones using the surface geochemical data. The variations of mineralization in the depth and the number of concealed mineralized zones are determined using FCM diagram.

FCM was performed on geochemical data based on the several steps as bellow [17]:

Step 1: 2DFT: The surface geochemical data were contoured using Kriging method and the geochemical distribution map was obtained. The geochemical distribution map is a continues map that can be considered as a two-dimensional function. The geochemical map of elements in the spatial domain was transformed to the frequency domain using 2DFT. Therefore, the PS map for all of elements were separately obtained.

Step 2: Designation and implementation of filter functions: Various filter functions were designed based on the PS map of mineralization element. The distribution of PS values in this map and the maximum and the minimum of wave numbers in the direction of X and Y are important for designation of these filters. The various filters consist low pass, band pass and high pass filters. These filter functions keep the certain wave numbers and eliminate the other wave numbers. These filters were performed on PS map only based on the wave number values without considering the PS values. Several frequency bands (FBs) were extracted from the geochemical distribution map using these filter functions.

Step 3: Determination of the mineralization component using PCA method:

The PCA method was performed on the PS data set consists of 39 elements to recognize the mineralization component. The behavior of mineralization elements and mineralization factor in the FBs was investigated individually. The factor scores of the rotated component matrix in PCA reveal the importance of mineralization phase in the FBs.

Step 4: Delineation of frequency coefficients diagram:

The deep and near surface mineralization zones commonly create the low and the high concentrations in the surface geochemical map, respectively [27]. The concentration of elements in the surface is related to the depth of mineral deposits [28]. The variety of frequency signals in the surface geochemical distribution map is also related to the intensity of depletion and enrichment of elements in the surface [15, 17]. The PCA scores in the rotated component matrix show the importance of elements in the FBs and the mineralization intensity. The frequency coefficients of mineralization elements (Y axis) that were obtained from the mineralization factor of PCA are delineated versus the FBs (X axis) in the FCM diagram. This diagram shows the importance of the mineralization elements in the FBs. The diagram can predict the deep situation of the mineralization zones and the variations of the concentration from the surface to the depth. The deep mineral deposits commonly create the weak anomalies in the surface and hence mostly cause low frequency signals in the surface geochemical distribution map. Therefore, the deep mineral deposits intensify the mineralization factor in the low FBs while the surface mineral deposits intensify the mineralization factor in the high FBs. In addition, the concealed mineralized zones can be discriminated from the deep disperse zones and the non-mineralized zones using this method.

3. Geology and mineralization of studied region

The Chichakloo Pb-Zn mineralization area is located in the northwest of Iran and around Zanzan city (Fig. 2). Geologically, the studied area is located in the contact of two tectonic zones of the Alborz-Azerbaijan and the Sanandaj-Sirjan. In this area, the outcrops of geological units are classified into three main units. The oldest geological unit, aged Precambrian that has outcrops in the south and the west of the area, includes mica and talc schist. The second unit, aged Paleozoic, has been formed from gray to white colored dolomites with brecciated texture [29].

The oldest carbonate unit is brown dolomite and contains chert bands. The silica veins and veinlets are increased toward the north in this unit. This dolomite unit in the western parts of the studied area has been interrupted by the minor faults with the northwest-southeast trend. In the middle and the western parts of the studied area, this unit contains relatively high amount of fine white calamine. This unit is considered as the host rock of the lead and zinc mineralization. This unit contains silica veins and veinlets and jasperoid bodies, and has extensive spread in the western and the northwestern parts of the studied area. The carbonated unit has been impressed by the faults and contains the white to cream dolomites. The youngest geological unit, aged Eocene, consists of sandstone and red colored shale. The Most of faults in this area are normal and strike slip type. These faults mainly shows a north-south trend [29].

The sand-breccia dolomite, the contact between the dolomite and the shale, and also, diagenetic processes and veinlet forms have important role in the mineralization. Tectonic processes such as the north-south faults have significant role in replacement of the metallic ores. Galena minerals are presented the inside of calcite and dolomite crystals. Sphalerite minerals and cubic pyrites are also observed with galena in the ore minerals. Lead and zinc primary minerals in the ground surface and shallow depth were converted to secondary minerals such as smithsonite, calamine and cerosite due to the weathering and the supergene processes [29].

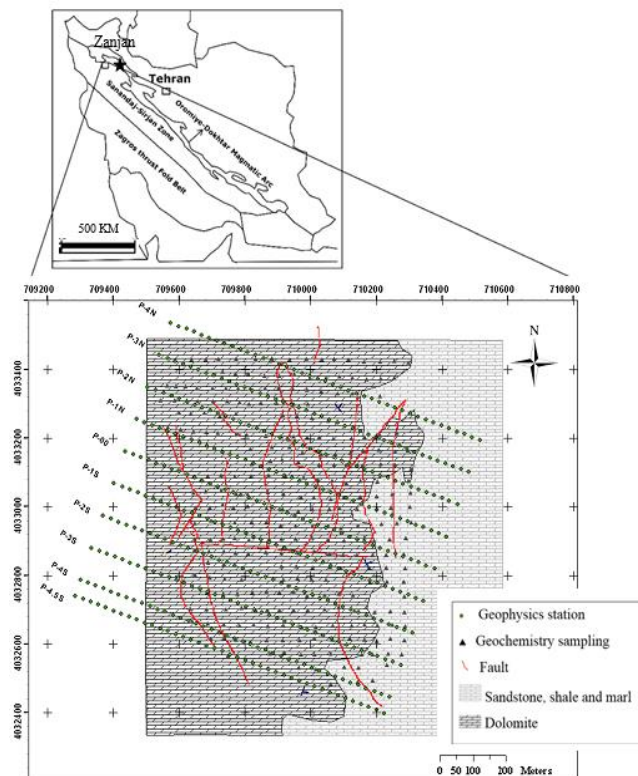


Fig. 2. The location and geological map of the studied area showing the geological units, faults, parallel geophysical exploration stations and the grid net of geochemical sampling

4. Implementation of proposed scenario on geochemical data

292 lithochemical samples were collected and analyzed for 39 elements in Chichakloo Pb – Zn mineralized area. The location of geochemical samples was illustrated in Fig. 3. The geochemical contour maps of Pb and Zn were obtained using the Kriging method (Fig. 3). The statistical characteristics of Pb and Zn elements in the surface lithochemical data were shown in table 1. The Pb and Zn geochemical distribution maps in the spatial domain were also shown in Fig. 4. The investigations in the frequency domain were performed based on these maps and the variations of concentrations.

Table 1. The statistical characteristics of Pb, Zn, Cu, Au, Ag and Mo elements of the surface lithochemical data

	Pb (ppm)	Zn (ppm)	Cu (ppm)	Au (ppb)	Ag (ppm)	Mo (ppm)
Mean	594.06	1165.00	29.98	12.13	1.28	2.28
Median	128.00	578.50	7.80	3.00	0.26	0.90
Mode	114	262.00	4.10	2.00	0.14	0.70
Std. Deviation	1895.17	1815.55	75.14	41.76	4.83	7.27
Skewness	6.18	3.20	6.37	8.81	10.00	9.27
Minimum	4.30	26.00	0.00	0.00	0.00	0.00
Maximum	19300.00	12700.00	753.00	542.00	67.00	90.80

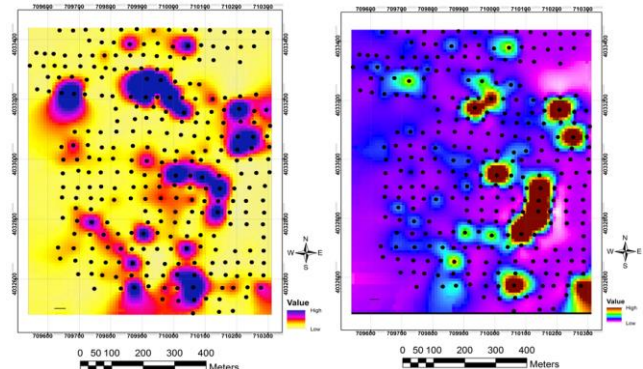


Fig. 3. The geochemical distribution map of Zn and Pb and the location of geochemical samples

The geochemical distribution map for all of 39 elements were separately plotted and these maps as two-dimensional images were transformed into the frequency distribution maps using 2DFT. The frequency distribution map of the surface geochemical data includes the power-spectrum (PS) values and wave numbers in the east – west and the north - south directions. The frequency distribution maps of Pb and Zn elements were depicted as the PS distribution maps in Fig. 4. These frequency maps illustrate high and low PS values related to low and high frequencies, respectively. Each point in the PS distribution map represents a particular geochemical frequency signal in the surface geochemical map. The high PS values are originally increased around the center of PS distribution map.

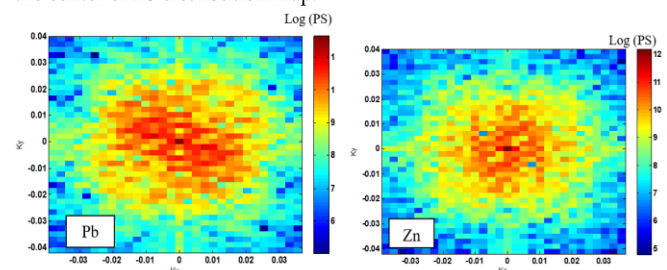


Fig. 4. The PS distribution maps of Pb and Zn elements obtained from the surface geochemical distribution map

10 different filters consisting low pass, band pass and high pass filters were designed based on the PS distribution map of the mineralization elements. The maximum and minimum of wave numbers and the PS

values are important in the filter designing (Table 2). These designed filters were applied for decomposing the PS distribution map for all of 39 elements, separately. The applied filter functions for FB4, 5, 8 and 9 were schematically shown for Pb element in Fig. 5.

Table 2. The designed filters in the frequency domain that are related to the various FBs

Designed Filter	
Frequency band 1	$G(k_x, k_y) = \begin{cases} 1 & k_x \geq 0.045 \text{ and } k_y \geq 0.045 \\ 0 & \text{otherwise} \end{cases}$
Frequency band 2	$G(k_x, k_y) = \begin{cases} 1 & k_x \geq 0.04 \text{ and } k_y \geq 0.04 \\ 0 & \text{otherwise} \end{cases}$
Frequency band 3	$G(k_x, k_y) = \begin{cases} 1 & k_x \text{ and } k_y \leq 0.04 \text{ and } \left\{ \begin{array}{l} 0.03 \leq k_x \leq 0.04 \\ \text{OR} \\ 0.03 \leq k_y \leq 0.04 \end{array} \right\} \\ 0 & \text{otherwise} \end{cases}$
Frequency band 4	$G(k_x, k_y) = \begin{cases} 1 & k_x \text{ and } k_y \leq 0.03 \text{ and } \left\{ \begin{array}{l} 0.02 \leq k_x \leq 0.03 \\ \text{OR} \\ 0.02 \leq k_y \leq 0.03 \end{array} \right\} \\ 0 & \text{otherwise} \end{cases}$
Frequency band 5	$G(k_x, k_y) = \begin{cases} 1 & k_x \text{ and } k_y \leq 0.02 \text{ and } \left\{ \begin{array}{l} 0.01 \leq k_x \leq 0.02 \\ \text{OR} \\ 0.01 \leq k_y \leq 0.02 \end{array} \right\} \\ 0 & \text{otherwise} \end{cases}$
Frequency band 6	$G(k_x, k_y) = \begin{cases} 1 & k_x \text{ and } k_y \leq 0.01 \text{ and } \left\{ \begin{array}{l} 0.005 \leq k_x \leq 0.01 \\ \text{OR} \\ 0.005 \leq k_y \leq 0.01 \end{array} \right\} \\ 0 & \text{otherwise} \end{cases}$
Frequency band 7	$G(k_x, k_y) = \begin{cases} 1 & k_x \text{ and } k_y \leq 0.005 \text{ and } \left\{ \begin{array}{l} 0.0025 \leq k_x \leq 0.005 \\ \text{OR} \\ 0.0025 \leq k_y \leq 0.005 \end{array} \right\} \\ 0 & \text{otherwise} \end{cases}$
Frequency band 8	$G(k_x, k_y) = \begin{cases} 1 & k_x \text{ and } k_y \leq 0.01 \\ 0 & \text{otherwise} \end{cases}$
Frequency band 9	$G(k_x, k_y) = \begin{cases} 1 & k_x \text{ and } k_y \leq 0.005 \\ 0 & \text{otherwise} \end{cases}$
Frequency band 10	$G(k_x, k_y) = \begin{cases} 1 & k_x \text{ and } k_y \leq 0.0025 \\ 0 & \text{otherwise} \end{cases}$

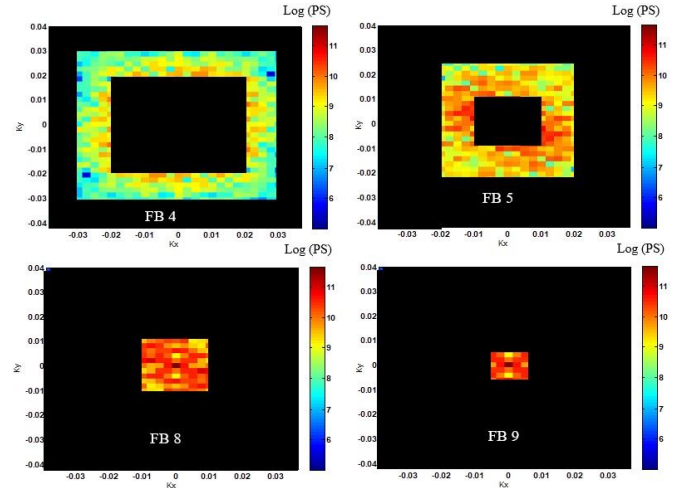


Fig. 5. The designed filters in the frequency domain for the FBs 4, 5, 8 and 9 and the PS maps of the Pb geochemical data

The variations intensity of the geochemical distribution map in the spatial domain is equivalent to the intensity of frequencies in the frequency domain. Therefore, the low variabilities in the spatial domain geochemical data are related to the low wave numbers and the high PS values in the central parts of PS map. Subsequently, the high variabilities in the geochemical map are related to the high frequencies that are distinguished with the high wave numbers and the low PS values in the frequency domain. The designed filter functions, $G(K_x, K_y)$, were performed on the PS distribution map and some wave numbers were eliminated. The PCA method was executed on the PS values for 39 elements in the decomposed FBs. Mineralization phases and their features were determined in each FB using the results of PCA method. The some obtained rotated component matrixes were represented in Tables 3, 4, 5, 6 and 7. The mineralization elements and the paragenesis elements and their principal components were distinguished for each FB.

Table 3. The rotated component matrix obtained from PCA in FB 3

	Component			
	1	2	3	4
Au	0.860	0.140	0.290	0.151
Cr	0.408	0.847	0.112	0.105
Mn	0.639	0.556	0.000	0.278
Ni	0.063	0.942	0.058	0.159
Pb	0.071	0.518	0.240	0.652
Sr	0.478	0.806	0.112	0.006
Ba	0.220	0.402	0.736	0.092
Be	0.660	0.210	0.682	0.055
Ti	0.716	0.352	0.592	0.004
Fe	-0.034	0.698	0.271	0.269
Al	0.410	0.282	0.851	0.042
Ca	0.576	0.757	0.079	0.056
Li	0.462	0.768	0.206	0.098
P	0.939	0.129	0.276	-0.007
V	0.744	0.222	0.618	0.000
Mg	0.340	0.819	0.421	0.082
K	0.954	0.208	0.193	-0.014
Na	0.379	0.041	0.865	0.035
S	0.825	0.083	0.330	0.056
Zr	0.272	0.149	0.940	0.031
Ag	0.108	0.306	0.394	0.766
As	0.792	0.083	0.071	0.433
Bi	0.751	0.563	0.013	0.040
Co	0.609	0.359	0.362	0.304
Cu	0.510	0.335	0.632	0.305
Mo	0.355	0.795	0.367	0.117
Sb	0.081	0.169	0.847	0.295
Zn	0.726	0.395	0.174	0.293

Sn	0.902	0.184	0.344	-0.038
W	-0.016	0.717	0.247	0.367
Cs	0.840	0.257	0.450	0.018
Nb	0.939	0.177	0.266	-0.032
U	0.855	0.102	0.279	0.121
Cd	0.531	0.392	0.006	0.568
Rb	0.892	0.253	0.355	0.000
Th	0.631	0.183	0.742	0.007
Y	0.048	0.782	0.341	0.091
Ce	0.294	0.313	0.840	0.026
Tl	0.024	0.097	-0.058	0.797

Table 4. The rotated component matrix obtained from PCA in FB 4

	Component					
	1	2	3	4	5	6
Au	0.440	0.624	-0.040	0.174	0.297	-0.004
Cr	0.080	0.387	0.766	0.071	0.076	0.108
Mn	0.430	0.547	0.203	0.094	0.345	-0.045
Ni	0.140	0.311	0.813	0.026	0.043	0.187
Pb	-0.065	0.690	0.101	0.277	0.104	0.334
Sr	0.398	0.526	0.287	0.002	0.008	-0.141
Ba	0.013	0.292	0.170	0.116	0.650	0.276
Be	0.814	0.166	0.107	0.152	0.268	-0.014
Ti	0.812	0.170	0.302	0.210	0.253	0.131
Fe	0.366	0.603	0.244	0.100	0.137	0.164
Al	0.624	0.171	0.139	0.700	0.084	0.050
Ca	0.491	0.188	0.635	0.005	0.183	0.259
Li	0.344	0.208	0.646	0.147	0.266	0.201
P	0.707	0.252	0.299	0.282	-0.068	0.235
V	0.799	0.170	0.197	0.393	0.185	0.157
Mg	0.463	0.352	0.586	0.133	0.298	-0.088
K	0.920	0.259	0.120	-0.056	0.051	0.061
Na	0.535	0.384	-0.158	0.331	-0.080	0.213
S	0.346	0.483	0.037	0.176	-0.146	0.455
Zr	0.537	0.084	0.045	0.769	0.068	0.082
Ag	0.288	0.738	0.289	-0.012	0.147	0.298
As	0.397	0.774	0.155	-0.128	0.151	0.105
Bi	0.340	0.695	0.404	-0.062	-0.070	-0.162
Co	0.208	0.207	0.347	0.098	0.220	0.622
Cu	0.009	0.707	0.355	0.241	0.059	0.180
Mo	0.109	0.611	0.354	0.333	0.283	-0.081
Sb	0.169	0.774	0.251	0.313	0.054	0.118
Zn	0.100	0.670	0.316	0.005	-0.031	0.293
Sn	0.838	0.306	0.165	-0.002	-0.137	0.170
W	0.224	0.522	0.382	0.053	0.385	0.034
Cs	0.828	0.214	0.142	0.154	0.265	0.082
Nb	0.899	0.181	0.203	0.005	0.151	0.157
U	0.206	0.272	0.220	0.026	0.360	0.681
Cd	0.380	0.692	0.015	-0.155	0.192	0.094
Rb	0.931	0.244	0.118	0.061	0.071	-0.006
Th	0.832	0.227	0.107	0.439	0.086	0.056
Y	0.257	0.120	0.135	0.008	0.789	0.084
Ce	0.627	0.174	0.328	0.513	0.185	0.191
Tl	0.304	0.718	0.088	0.080	0.400	0.177

Table 5. The rotated component matrix obtained from PCA in FB 5

	Component						
	1	2	3	4	5	6	7
Au	0.081	0.154	-0.018	-0.056	0.561	0.378	-0.109
Cr	0.475	0.453	0.472	0.112	-0.056	0.102	0.010
Mn	-0.003	0.035	0.121	0.805	0.107	0.199	0.161
Ni	0.318	0.365	0.675	0.233	0.142	0.017	0.163
Pb	0.145	0.817	0.024	0.060	-0.102	-0.002	0.354
Sr	0.154	0.485	0.091	0.394	0.520	-0.056	0.088
Ba	0.217	-0.008	0.073	-0.010	0.715	0.011	0.261
Be	0.786	0.060	0.075	0.016	0.063	0.201	0.483

Ti	0.931	0.172	0.047	0.036	0.130	0.026	0.134
Fe	0.275	0.768	0.270	-0.063	0.102	0.016	0.002
Al	0.882	0.142	0.210	-0.039	0.228	0.022	0.190
Ca	0.762	0.377	0.208	0.188	0.118	0.036	0.057
Li	0.381	0.239	0.292	0.347	0.564	0.021	-0.092
P	0.707	0.248	0.497	0.096	0.092	0.071	-0.009
V	0.937	0.152	0.168	0.029	0.047	0.035	0.057
Mg	0.739	0.154	0.171	0.049	0.260	0.033	0.413
K	0.929	0.065	0.053	0.090	0.032	0.101	-0.129
Na	0.405	-0.001	0.097	0.171	0.116	0.179	0.794
S	0.154	0.473	0.157	0.608	-0.084	0.107	-0.160
Zr	0.806	0.041	0.023	-0.085	0.135	0.079	0.484
Ag	0.133	0.914	0.115	0.082	-0.025	-0.010	0.025
As	0.066	0.826	0.056	0.038	0.360	-0.008	-0.185
Bi	0.179	0.517	0.317	0.276	0.038	-0.010	0.357
Co	0.167	0.082	0.821	0.170	0.139	0.015	0.010
Cu	0.221	0.705	0.096	0.264	0.029	0.355	0.027
Mo	0.202	0.463	0.078	0.528	0.027	0.027	0.106
Sb	0.083	0.815	0.059	0.055	0.085	0.223	-0.078
Zn	0.040	0.352	0.116	0.258	0.024	0.753	0.104
Sn	0.790	0.240	0.107	0.240	-0.046	-0.086	0.096
W	0.465	0.341	0.256	0.046	0.206	0.068	-0.048
Cs	0.851	0.247	0.305	0.043	-0.067	0.014	-0.052
Nb	0.925	0.176	0.034	0.134	0.063	-0.003	0.051
U	0.214	0.199	0.803	-0.019	-0.010	0.222	0.070
Cd	0.051	-0.017	0.110	0.053	0.129	0.849	0.091
Rb	0.957	0.073	0.088	0.040	0.043	0.082	-0.015
Th	0.931	0.123	0.074	-0.014	0.079	0.006	0.137
Y	0.579	-0.015	0.182	0.122	0.376	0.246	0.066
Ce	0.821	0.104	0.137	0.142	0.231	-0.115	0.040
Tl	0.308	0.614	0.266	0.378	0.192	-0.043	-0.041

Table 6. The rotated component matrix obtained from PCA in FB 7

	Component			
	1	2	3	4
Au	-0.163	0.024	0.912	-0.245
Cr	0.988	0.130	-0.055	0.010
Mn	0.680	0.548	-0.115	-0.151
Ni	0.991	0.128	-0.011	0.013
Pb	0.357	0.832	-0.070	0.123
Sr	0.195	0.219	0.882	0.274
Ba	0.883	0.361	-0.232	0.009
Be	0.961	-0.015	0.000	-0.033
Ti	0.993	0.109	0.011	-0.015
Fe	0.942	0.279	0.128	-0.020
Al	0.991	0.098	-0.005	0.029
Ca	0.993	0.107	-0.018	0.002
Li	0.987	0.095	-0.024	0.054
P	0.993	0.104	0.011	-0.009
V	0.990	0.134	0.005	-0.006
Mg	0.989	0.138	0.003	0.009
K	0.991	0.121	0.027	-0.014
Na	0.952	0.115	0.153	-0.137
S	0.796	0.002	-0.376	-0.047
Zr	0.991	0.077	-0.003	0.030
Ag	0.334	0.809	0.381	0.107
As	-0.029	0.809	0.532	-0.147
Bi	0.924	0.103	0.268	0.017
Co	0.983	0.175	-0.034	0.006
Cu	-0.163	-0.071	-0.003	0.968
Mo	0.840	-0.341	-0.224	-0.225
Sb	-0.447	0.774	-0.045	-0.158
Zn	0.819	0.212	-0.163	0.350
Sn	0.991	0.119	0.039	-0.023
W	0.970	0.207	-0.097	0.036
Cs	0.993	0.090	0.000	-0.011
Nb	0.990	0.118	0.038	-0.034

U	0.938	0.218	-0.007	-0.116
Cd	0.795	0.084	-0.138	0.386
Rb	0.991	0.123	0.026	-0.010
Th	0.988	0.132	0.009	0.010
Y	0.982	0.074	0.071	0.005
Ce	0.989	0.076	-0.047	0.014
Tl	0.658	0.711	-0.044	0.001

Table 7. The rotated component matrix obtained from PCA in FB 8, 9

	FB8			FB9	
	1	2		1	2
Au	0.877	0.433	Au	0.884	0.432
Cr	0.740	0.669	Cr	0.743	0.668
Mn	0.868	0.490	Mn	0.871	0.488
Ni	0.597	0.800	Ni	0.600	0.800
Pb	0.824	0.495	Pb	0.839	0.527
Sr	0.878	0.471	Sr	0.880	0.471
Ba	0.728	0.676	Ba	0.735	0.671
Be	0.721	0.676	Be	0.733	0.665
Ti	0.483	0.875	Ti	0.480	0.877
Fe	0.718	0.692	Fe	0.725	0.687
Al	0.521	0.851	Al	0.521	0.852
Ca	0.859	0.505	Ca	0.861	0.505
Li	0.556	0.828	Li	0.557	0.828
P	0.607	0.794	P	0.608	0.794
V	0.628	0.777	V	0.630	0.776
Mg	0.833	0.548	Mg	0.835	0.548
K	0.519	0.854	K	0.519	0.855
Na	0.310	0.923	Na	0.304	0.933
S	0.744	0.638	S	0.750	0.638
Zr	0.506	0.847	Zr	0.510	0.859
Ag	0.807	0.529	Ag	0.825	0.530
As	0.848	0.467	As	0.861	0.456
Bi	0.717	0.664	Bi	0.738	0.655
Co	0.682	0.728	Co	0.687	0.726
Cu	0.880	0.458	Cu	0.888	0.452
Mo	0.750	0.615	Mo	0.763	0.623
Sb	0.894	0.419	Sb	0.909	0.407
Zn	0.831	0.548	Zn	0.832	0.551
Sn	0.545	0.837	Sn	0.546	0.838
W	0.689	0.717	W	0.690	0.722
Cs	0.533	0.844	Cs	0.533	0.845
Nb	0.477	0.878	Nb	0.475	0.880
U	0.849	0.522	U	0.852	0.521
Cd	0.696	0.642	Cd	0.728	0.637
Rb	0.536	0.843	Rb	0.537	0.844
Th	0.578	0.815	Th	0.579	0.815
Y	0.830	0.551	Y	0.833	0.550
Ce	0.656	0.752	Ce	0.661	0.748
Tl	0.728	0.626	Tl	0.745	0.638

5. Results, discussion and evaluation:

Cheng (2012) demonstrated the concentration of elements in the surface is a function of the depth of mineral deposits [28]. He showed the outcropping and shallow ore deposits create the large concentration in the surface while the ore deposits occurred about 1 km subsurface, they show small concentrations in the surface [27]. This fact indicates the deep mineral deposit can create the low frequency signals at the surface geochemical distribution map. Zuo and Wang (2015) presented a simulated geochemical pattern contains the ore deposits in different burial depths. They demonstrated the deeper ore deposit shows a weaker concentration map on the surface and this distribution map contains the low frequency signal that are not almost distinguishable from the background [15]. The surface ore deposit can create the high

frequency signals and the deep ore deposit create the low frequency signals in the surface geochemical data. The FCM surveys the behaviors of mineralization process in various FBs and their relationships with the mineralized zones at different depths.

The PCA as a dimension reduction method has divided the 39 elements to the 9 principal components (PC) in the FB1. The PC2, which were recognized as the mineralization component, consists of Pb, Zn and Cd elements. In this FB with very high frequency signals, the geochemical mineralization pattern was properly distinguished from the geochemical background and noises. Therefore, the FBs with the high frequency signals can also consist the mineralization effects. The mineralization components in these FBs are commonly related to the surface mineralization. Hence, this obtained mineralization pattern demonstrates a Pb and Zn mineralization in the surface. The field observations and the surface mineralization confirm this fact.

The PCA has divided the 39 elements into the 9 PCs in FB2 (high frequency band) and the mineralization elements are shown in the PC2 and PC6. The PC2 consists the elements of Pb, Ag, Mo, Sb and Tl while the elements of Zn and Cd are together in the PC6. The PCA has divided the 39 elements into the 4 PCs in the FB3 (Table 3). The elements of Pb, Ag, Cd and Tl are together in the PC4 while Zn was separated in the PC1. The 39 elements were divided into the 6 PCs in the FB4 (table 4). Pb and Zn are related to Au, Mn, Sr, Fe, Ag, As, Bi, Cu, Mo, Sb, W, Cd and Tl in the PC2. The PCA has divided the 39 elements into 7 PCs in the FB5 (table 5). PC2 as the mineralization component consists of Pb, Fe, Ag, As, Bi, Cu, Sb and Tl while the elements of Zn and Cd are in the PC6 as the second mineralization component. The PCA has also divided the 39 elements into 7 PCs in the FB6. The elements of Pb, Ba, Ag, As, Bi and Tl were detected in PC2 as the first mineralization component and the elements of Cu, Cd and Zn are related together in PC4 as the second mineralization component. In the FB7, the elements of Pb, Sb, Mn, Ag, As and Tl are related to the mineralization phase (PC2) and Zn was divided with most elements in PC1 as the background factor (table 6). The geochemical patterns such as mineralization phase, includes Zn and Pb, could not be separated from other elements in the FB 8 and 9 (table 7). The mineralization component was not revealed properly in these low FBs and the behavior of Pb and Zn is similar to the other elements. The FB10 includes the largest PS values and the very low frequency signals. The all 39 elements have similar behavior and dispersion in this FB and the PCA has divided these elements into one component as the background factor. The geochemical background factor that is related to the regional geological effects and the deep mineralized zones can cause the low frequency signals in the surface geochemical distribution map. There is an important relationship between the depth of mineralized zones and the distribution of frequency signals in the surface geochemical map. The results of the FB10 show there is not mineralization factor in the very low FB and hence there is not any frequency effect of very deep mineralization in the surface geochemical data in this area.

The frequency coefficients of mineralization and paragenesis elements obtained from the PCA are directly related to the extension of mineralization process. The FCM diagram is plotted using these frequency coefficients in the Y axis versus the FBs in the X axis. This diagram for Zn and Pb, in the frequency domain was depicted in Chichacloo area (Fig. 7). The variations of mineralization process in the various FBs are delineated and shown using the FCM diagram. The FCM diagram can illustrate the variations trend of mineralization process from low frequency to high frequency geochemical signals. The situation of hidden mineralization zones in the various depths can be predicted using the intensity of the mineralization processes in the FBs. The FCM diagram shows two distinctive frequency anomalies with high frequency coefficients in the high and intermediate FBs for the Zn and Pb elements. These frequency anomalies are related to geochemical anomalies in the spatial domain. Therefore, there are a surface Zn–Pb mineralized zone related to the frequency anomaly in the high FBs and a hidden Zn–Pb mineralized zone in the moderate depth that has created the frequency anomaly in the moderate FBs. There is no frequency anomaly in the low FBs based on the FCM diagram. This demonstrates there is not a very deep mineral deposit in this area to

create the frequency anomaly in the low FBs.

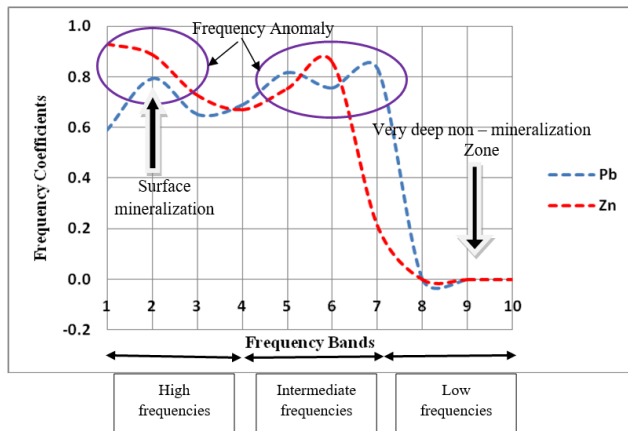


Fig. 6. The FCM diagram of Pb and Zn in the different FBs shows two frequency anomalies

The first frequency anomaly in the high FBs shows a surface geochemical anomaly and a surface mineralized zone in the spatial domain. The surface exploratory information demonstrates that there is a surface mineralized zone in this area. The results of the FCM show Zn plays more important role than Pb in high FBs. This subject is proved and confirmed by the surface geochemical data and Zn has the higher mean, median and mode concentrations than Pb in the surface geochemical data. The mean and mode values of Zn in the surface are approximately twice the amounts of Pb (table 1).

Geophysical data were processed and modeled to examine the accuracy and validity of the FCM method for prediction of the situation of mineralization in the depth. Dipole-dipole electrode configuration was used in this study and 10 parallel lines with a distance of 100 meters from each other were established in the dolomite unit (Fig. 2). Along the lines in the surveys, the dipoles with a spacing of 75 meters and electrodes movement of 25 meters with the distance between the centers of the dipoles of minimum 2×75 meters and maximum 6×75 meters were considered.

We used the RES2DINV software and a smoothness-constrained least squares method to invert IP and resistivity data. Prior to modeling, all data were manually edited by rejecting the noisy measurements. In general, the IP data have very high quality in the all profiles, but the resistivity data show more noise measurements. There is sufficient convergence without over fitting the data between three to five iterations of the inversions. The RMS errors of resistivity models range from 10% (P-1N) to 29.7% (P-4.5S), while the RMS errors of IP models do not exceed from 5% in the all profiles. Although a larger number of iterations can decrease the RMS error, it causes distortions in the models when we tried to reduce the data misfit below this level. It is worth mentioning that the higher RMS error of resistivity models is due to the large resistivity variations along the profiles.

Fig. 7 shows two examples of the inverse modeling results of the resistivity and IP data for the P-4N and P-4.5S. The P-4N was selected from the north of the studied area which appears to be almost sterile in the mineralization while the P-4.5S was selected from the south of the studied area where the high geophysical and geochemical anomalies were observed. The modeling results of the P-4N shows the presence of a zone with a chargeability of more than 10 milliseconds (slightly greater than background) in the middle of profile and coincides with the dolomite unit with a great extent from the near surface. The resistivity of this zone is less than 150 ohm-meters which is significantly lower than the resistivity of the dolomite unit. The modeling results for the profile P-4.5S reveals the presence of an anomaly with a chargeability of more than 35 milliseconds and the lateral extent from 0 to 225 m along the profile at the depth of 10 to 60 m. The resistivity of this anomaly is varying but it reduced to less than 250 ohm-meters at lateral extent of 125 to 225m along the profile. The resistivity variations of the anomaly can imply varying mineralization texture of the anomaly, which is

located in the dolomite unit as the host rock. Another anomaly with a chargeability of around 30 milliseconds can be observed at the lateral extent of 400 to 600 m along the profile and depth extent of 30 to 70 m. The resistivity of this anomaly is generally low but relatively varying since shale, sandstone and clay accompany the anomaly.

The modeling results of other profiles (not shown here) show a similar pattern of resistivity and IP variations. Two different and distinctive resistivity zones can be distinguished in the resistivity models. One of the two zones, having a resistivity of greater than 700 ohm-meters, is located in the west part of the map and is embedded in the dolomite unit. The extension of this zone from the north to the south is evident in the resistivity models and is consistent with the geology map. The other zone, having a resistivity of less than 150 ohm-meters, is located in the east part of the map and is embedded in the marl, sandstone and shale units. In the IP models, the extended IP anomalies are mainly observed from the near surface to the intermediate depth (less than 100m). A significant decrease in the chargeability and extension of the IP anomalies is quite evident from the south to the north so the chargeability in the northern part falls below 15 milliseconds.

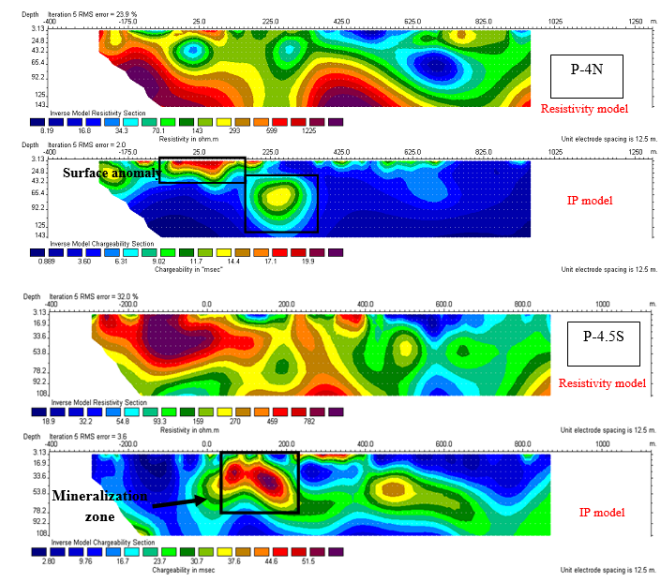


Fig. 7. 2D inverse model of resistivity and IP sections for the profiles P-4N and P-4.5S.

The results of resistivity and IP data modelling properly confirm the results of FCM. Two frequency anomalies were obtained using the FCM diagram. These frequency anomalies show a mineralized zone in the surface and a weak mineralized zone at the intermediate depths. The geophysical models show a surface geophysical anomaly related to the first frequency anomaly in the FCM diagram. The results of geophysical surveys also show relatively high geophysical anomalies at the intermediate depths (Fig. 7). The resistivity of this zone is less than the dolomite unit. This geophysical anomaly with a chargeability more than 35 milliseconds is shown at the depth of 10 to 60 m.

The drilled boreholes properly confirm the results of FCM and geophysical models. The drilled borehole 06 has also detected the intermediate mineralized zone approximately from 40 up to 70 meter at the depth (Fig. 8). This mineralization zone consists the fine crystals of galena and sphalerite that are associated with iron hydroxide and dark matrix.

The FCM diagram has not illustrated any frequency anomaly in low FBs so this method demonstrates no mineralized zone in very deep parts of Chichakloo area. The geophysical models and the drilled boreholes also show the presence of non-mineralized zone at high depth and confirm properly the results of FCM. As shown in Fig. 9, these drilled boreholes show a mineralized zone in the near surface and a non-mineralized zone in the high depth. This advanced technique can distinguish the mineralized and non-mineralized zones in the depth

without necessity to the exploration drilling. The introduced methodology, based on the 2DFT, is quite inexpensive in comparison with the traditional exploration methods. Interpretation of the geochemical data in the frequency domain can provide important achievements about the mineral deposits and significant implications for the mineral exploration.

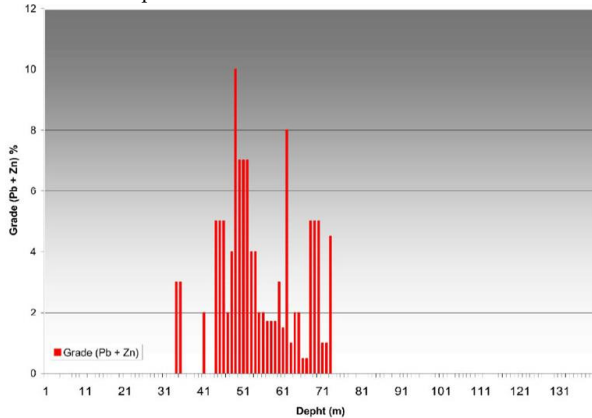


Fig. 8. The drilled borehole 06 has detected the mineralized zone at the intermediate depth

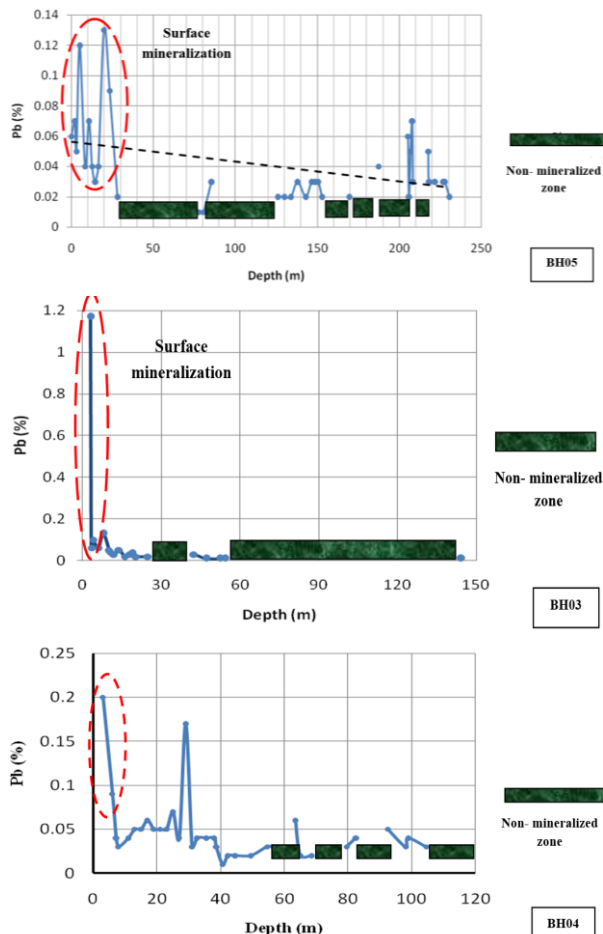


Fig. 9. Distribution of Pb concentration at the depth in borehole BH03, BH05 and BH04 – there is a non-mineralized zone at the depth

6. Conclusion

In this study, the surface geochemical data in Chichakloo Pb–Zn mineralization area were interpreted in the frequency domain using FCM. New exploratory information about the hidden ore deposits can

be acquired using the interpretation of surface geochemical data in the frequency domain. In this paper, the surface geochemical distribution maps for all of 39 elements were decomposed to the various frequency signals using 2DFT. The frequency signals were divided into the 10 frequency bands based on the 10 filter functions consisting of the low pass, band pass and high pass filters. The behaviors of any elements specially Pb and Zn mineralization elements in any frequency bands were surveyed using the PCA. The frequency coefficients of Pb and Zn elements in each FB were extracted from the PCA rotated component matrix and the FCM diagram was delineated. The FCM can properly distinguish the behavior of mineralization process in various frequency bands and predict the situation of mineralization in the depth. The shallow ore deposits generally create the large concentration in the surface while the deep ore deposits mostly cause the low surface anomaly and create the low geochemical frequency signals in the surface. Some of these deep mineralization elements hold low concentration in the surface same as geochemical background, therefore the effects of mineralization can just be detected in low geochemical frequency signals. The FCM diagram shows two frequency anomalies for Pb and Zn in the low and moderate frequency bands related to the surface and moderate depths of geochemical anomalies in the spatial domain. The FCM diagram shows there is not any frequency anomaly in the very low frequency bands. It demonstrates that the frequency behavior of Pb and Zn mineralization elements are similar to the background elements and there is a non-mineralization zone at the high depths. FCM predicted two mineralized zones at the surface and moderate depth and a non-mineralized zone at high depths in the studied area. The achieved interesting results of FCM have been corroborated by the results of surface mineralization, exploratory drilled borehole and geophysical models. The interesting presented method as a new pattern recognition technique reveals the significant information about the variations of mineralization in the depth.

REFERENCES

- [1] Ghezlbash, R., Maghsoudi, A., & Carranza, E. J. M. (2019). Performance evaluation of RBF-and SVM-based machine learning algorithms for predictive mineral prospectivity modeling: integration of SA multifractal model and mineralization controls. *Earth Science Informatics*, 1-17.
- [2] Parsa, M., Maghsoudi, A., Yousefi, M., & Carranza, E. J. M. (2017). Multifractal interpolation and spectrum–area fractal modeling of stream sediment geochemical data: implications for mapping exploration targets. *Journal of African Earth Sciences*, 128, 5-15.
- [3] Cao, L., Cheng, Q. (2012). Quantification of anisotropic scale invariance of geochemical anomalies associated with Sn-Cu mineralization in Gejiu, Yunnan Province, China. *Geochemical Exploration* 122, 47–54.
- [4] Fyzollahhi, N., Torshizian, H., Afzal, P., & Jafari, M. R. (2018). Determination of lithium prospects using fractal modelling and staged factor analysis in Torud region, NE Iran. *Journal of Geochemical Exploration*, 189, 2-10.
- [5] Zuo, R. (2011). Identifying geochemical anomalies associated with Cu and Pb–Zn skarn mineralization using principal component analysis and spectrum–area fractal the Gangdese Belt, Tibet (China). *J. Geochemical Exploration*. 111, 13-22.
- [6] Zuo, R. (2011). Decomposing of mixed pattern of arsenic using fractal model in Gangdese belt, Tibet, China. *Applied Geochemistry* 26, S271-S273.
- [7] Zuo, R., Carranza, E.J.M. & Cheng, Q. (2012). Fractal/multifractal modelling of geochemical exploration data. *Journal of Geochemical Exploration* 122, 1-3.
- [8] Zuo, R., Xia, Q. & Zhang, D. (2013). A comparison study of the C-A

- and S-A models with singularity analysis to identify geochemical anomalies in covered areas. *Applied Geochemistry* 33, 165-172.
- [9] Ghezlbash, R., Maghsoudi, A., & Daviran, M. (2019). Combination of multifractal geostatistical interpolation and spectrum–area (S–A) fractal model for Cu–Au geochemical prospects in Feizabad district, NE Iran. *Arabian Journal of Geosciences*, 12(5), 152.
- [10] Shokouh Saljoughi, B., Hezarkhani, A., & Farahbakhsh, E. (2018). A comparative study of fractal models and U-statistic method to identify geochemical anomalies; case study of Avanj porphyry system, Central Iran. *Journal of Mining and Environment*, 9(1), 209-227.
- [11] Zuo, R., Wang, J. (2015). Fractal/multifractal modeling of geochemical data: A review. *Journal of Geochemical Exploration*
- [12] Wang, H., Zuo, R. (2015). A comparative study of trend surface analysis and spectrum–area multifractal model to identify geochemical anomalies. *Journal of Geochemical Exploration*, 155, 84-90
- [13] Wang, J., Zuo, R. (2015). A MATLAB-based program for processing geochemical data using fractal/multifractal modeling. *Earth Science Informatics*, 1-11
- [14] Shahi, H., Ghavami, R., Kamkar Rouhani, A. & Asadi-Haroni, H. (2014). Identification of mineralization features and deep geochemical anomalies using a new FT-PCA approach, *Journal of Geopersia*, 4 (2), 101-110
- [15] Shahi, H., Ghavami Riabi, R., Kamkar Ruhani, A. & Asadi Haroni, H. (2015). Prediction of mineral deposit model and identification of mineralization trend in depth using frequency domain of surface geochemical data in Dalli Cu-Au porphyry deposit. *Journal of Mining and Environment*, 6(2), pp.225-236
- [16] Shahi, H., Ghavami, R., Kamkar Rouhani, A. & Asadi-Haroni, H. (2015). Application of Fourier and wavelet approaches for identification of geochemical anomalies, *Journal of African Earth Sciences* 106. 118–128
- [17] Shahi, H., Ghavami, R., & Rouhani, A. K. (2016). Detection of deep and blind mineral deposits using new proposed frequency coefficients method in frequency domain of geochemical data. *Journal of Geochemical Exploration*
- [18] Roberts, R.G., Sheahan, P., Cherry, M.E. (Eds.), (1988). *Ore deposit models: Geoscience Canada Reprint Series 3*. Geological Association of Canada, Newfoundland. 200 p
- [19] Cox, D.P., Singer, D.A. (Eds.), (1986). *Mineral Deposit Models*. U.S. Geological Survey Bulletin 1693. U.S. Government Printing Office, Washington. 379 p
- [20] Carranza, E.J.M., Sadeghi, M. (2012). Primary geochemical characteristics of mineral deposits - Implications for exploration, *Ore Geology Reviews* 45.1–4
- [21] Grigorian, S.V. (1985). *Secondary Lithochemical Halos in Prospecting for Hidden Mineralization*. Nedra Publishing House, Moscow
- [22] Grigorian, S.V. (1992). *Mining Geochemistry*. Nedra Publishing House, Moscow
- [23] Hassani, H., Daya, A., Alinia, F. (2009). Application of a fractal method relating power spectrum and area for separation of geochemical anomalies from background. *Aust J Basic Appl Sci*, 3(4), 3307-3320
- [24] Hornak, J. (1997). "The Basic of NMR." <http://www.cis.rit.edu/htbooks/nmr/inside.htm>.
- [25] Dobrin, M. B., Savit, C. H. (1988). *Geophysical prospecting*: McGraw-Hill Book Co., New York, 867 p
- [26] Bhattacharyya, B.K. (1966). Continuous spectrum of the total-magnetic-field anomaly due to a rectangular prismatic body. *Geophysics*, 31(1), 97-121
- [27] Cheng, Q. (2012). Singularity theory and methods for mapping geochemical anomalies caused by buried sources and for predicting undiscovered mineral deposits in covered areas. *Journal of Geochemical Exploration*, 122, 55-70
- [28] Cheng, Q. (2014). Vertical distribution of elements in regolith over mineral deposits and implications for mapping geochemical weak anomalies in covered areas. *Geochemistry: Exploration, Environment, Analysis*, 14(3), 277-289.
- [29] Farzamian, M., Rouhani, A. K., Yarmohammadi, A., Shahi, H., Sabokbar, H. F., & Ziaie, M. (2016). A weighted fuzzy aggregation GIS model in the integration of geophysical data with geochemical and geological data for Pb–Zn exploration in Takab area, NW Iran. *Arabian Journal of Geosciences*, 9(2), 104.